Advances in Geo-Energy Research

Vol. 20, No. 1, p. 56-70, 2026

Original article

Effects of energy-input mode on permeability enhancement of reservoir rock via low-amplitude stress waves

Zheng Wang[1], Geli Zhao[2], Ying Xu[1], Ling Yang[3], Bangbiao Wu[1]*, Kaiwen Xia[1,4]*

[1]*State Key Laboratory of Hydraulic Engineering Intelligent Construction and Operation, School of Civil Engineering, Tianjin University, Tianjin 300072, P. R. China*

[2]*Yalong River Hydropower Development Company, Ltd., Chengdu 610065, P. R. China*

[3]*Centre for Audio, Acoustics and Vibration, Faculty of Engineering and IT, University of Technology Sydney, Sydney NSW 2007, Australia*

[4]*State Key Laboratory of Deep Earth Exploration and Imaging, School of Engineering and Technology, China University of Geosciences (Beijing), Beijing 100083, P. R. China*

Keywords:
Permeability enhancement
stress wave loading
coupled hydraulic-mechanical loading
split Hopkinson pressure bar
rock dynamics

Cited as:
Wang, Z., Zhao, G., Xu, Y., Yang, L., Wu, B., Xia, K. Effects of energy-input mode on permeability enhancement of reservoir rock via low-amplitude stress waves. Advances in Geo-Energy Research, 2026, 20(1): 56-70.
https://doi.org/10.46690/ager.2026.04.05

Abstract:
Stress-wave stimulation offers a promising strategy for enhancing permeability in deep reservoir rocks, yet the governing mechanisms and influences of loading characteristics remain poorly understood. To address this shortcoming, in this study, controllable stress waves were applied to green sandstone specimens using a modified triaxial split Hopkinson pressure bar system under coupled hydraulic–mechanical loading conditions. Three distinct energy-input modes, including progressively increasing, constant, and progressively decreasing, were designed to deliver identical total energy through seven impacts. *In-situ* permeability was measured after each impact, and the corresponding dynamic response was analyzed to clarify the mechanisms of permeability evolution. The results showed that stress wave loading substantially enhances permeability, while the evolution trend strongly depends on the energy-input patterns and coupled hydraulic-mechanical conditions. Moreover, energy-constant loadings produce the most pronounced and sustained permeability growth, whereas energy-decreasing loadings yield sharp early increases followed by reductions due to compaction. Energy-increasing loading leads to delayed permeability enhancement, governed by the eventual onset of macro failure. Hydraulic pressure promotes permeability by facilitating fracture extension, while confining pressure inhibits crack propagation. The mechanical response parameters such as peak stress, peak strain and dissipated energy cannot consistently reflect permeability evolution due to their dependence on instantaneous loading. In contrast, residual deformation correlates strongly with permeability across different loading modes, serving as a reliable indicator of damage-induced fluid transport. This work clarifies the role of energy-input patterns in enhancing permeability and provides guidance for optimizing stress wave stimulation strategies in deep geo-energy recovery.

1. Introduction

Enhancing the permeability of deep reservoir rocks through external stimulation is essential for improving resource extraction efficiency (Lei et al., 2016; Ranjith et al., 2017; Jiang et al., 2024). Among the available techniques, stress wave loading has attracted growing interest due to its wide applicability and economic advantages (Mullakaev et al., 2015; Fan et al., 2024). However, the effectiveness of this approach inherently depends on loading characteristics, and the govern-

Yandy Scientific Press

*Corresponding author.
E-mail address: wangz0699@tju.edu.cn (Z. Wang); 10207271@sdic.com.cn (G. Zhao); maggie_xu@tju.edu.cn (Y. Xu); Ling.Yang-3@student.uts.edu.au (L. Yang); bbwu@tju.edu.cn (B. Wu); kaiwen.xia@cugb.edu.cn (K. Xia).

Received January 19, 2026; revised February 20, 2026; accepted March 12, 2026; available online March 15, 2026.

ing mechanisms remain insufficiently understood. Thus, identifying the key factors that govern permeability enhancement under stress-wave loading is critical for optimizing loading parameters and improving implementation strategies.

Previous investigations into permeability enhancement induced by directional stress waves have employed diverse loading techniques, with particular emphasis on parameters such as impact energy and frequency. Beyond these parametric effects, the broader evolution of this research field has been shaped by fundamental distinctions in stress wave generation methods and the role of the hydraulic condition. One major category of studies utilize high-voltage electrical discharges in water to generate shock waves, with early experiments on cylindrical mortar specimens revealing a permeability threshold beyond which enhancement becomes pronounced and positively correlates with shock count (Maurel et al., 2010). Subsequent modifications, such as initiating discharges within a central borehole, have demonstrated that the threshold amplitude increases with confining pressure, and they further established an exponential relationship between permeability evolution and loading cycles in coal samples (Chen et al., 2012; Zhao, 2022). Other variants of this approach, including electrical exploding wires for unplugging applications as well as the combination of discharge-induced wave loading with hydraulic fracturing, have confirmed that intrinsic permeability is jointly governed by injection pressure and confinement (Wang et al., 2021a; Duan et al., 2024) However, in these studies, water functions solely as a wave propagation medium and the influence of hydraulic conditions is not intrinsically incorporated, complicating mechanistic interpretation. To examine the evolution of intrinsic permeability caused by stress wave loading, researchers employed a split Hopkinson pressure bar (SHPB) to apply loads to specimens. This impact-based method generates stress waves in a more direct manner, thus eliminating the need for water. Early SHPB-based studies reported monotonic increases in both porosity and permeability with higher loading cycles and wave amplitudes in rock specimens (Yan et al., 2018; Jiang et al., 2019). To further elucidate the hydraulic effects, Zhao (2022) and Chen et al. (2024) successively modified the triaxial SHPB system by incorporating a hydraulic loading cell and facilitating a complete seepage channel. Wang et al. (2025c) subsequently employed this enhanced system to investigate the permeability enhancement of repeated stress waves under varying coupled hydraulic-mechanical (CHM) pressures, and they proposed a theoretical model describing the increasing-decreasing-stabilizing trend over a wide loading range.

Given the demonstrated dependence of permeability on both impact amplitude and loading cycles, the pattern of energy input, i.e., the amplitude order in cyclic loading, emerges as a comprehensive representation factor governing crack evolution and fluid transportation. Previous studies have examined permeability changes under controlled cyclic loading modes, including monotonic increases (Zhang et al., 2020; Sheng et al., 2021; Xu et al., 2025), constant-amplitude cycles (Kluge et al., 2021; Wang et al., 2025a; Wen et al., 2025), and sequential increase-decrease schemes (Zhou et al., 2020; Kozhevnikov et al., 2024a; Kozhevnikov et al., 2024b). These efforts revealed distinct permeability evolution behaviors associated with the timing (stress state) and degree of damage accumulation (Liu and Dai, 2021). However, it should be noted that existing studies are limited to quasi-static conditions, where loading is applied continuously and deformation develops gradually; the dynamic response of the material and the change of pore pressure cannot be incorporated into these analyses. In contrast, Wang et al. (2025c) have revealed certain trends in stress wave loading under the CHM condition. Nevertheless, systematic research on the influence of the energy input pattern itself, specifically the amplitude sequence, remains lacking.

To bridge this knowledge gap, this study utilizes the modified triaxial SHPB system to achieve controllable stress wave loading under varying CHM pressures. Seven impacts with consistent total energy input in energy-increasing, energy-constant, and energy-decreasing loading modes were conducted on green sandstone specimens. The inherent permeability of rock was measured *in-situ* after each impact and the corresponding dynamic response was derived to explore the damage evolution. The variations in permeability evolution between different loading modes and the connection between permeability and dynamic response were discussed. This work aims to elucidate the influence of energy input pattern on the permeability enhancing effect, providing novel insights for the stress wave loading design.

2. Material and methodology

2.1 Specimen processing

The specimen utilized in this study was processed from a raw block quarried from Southwest China. The mineral composition was tested using the electron probe micro analysis technique, with the results shown in Fig. 1. The study was conducted in accordance with the methodology outlined by the International Society for Rock Mechanics and Rock Engineering for the assessment of dynamic properties of rock materials (Zhou et al., 2012). A series of cylinders with a diameter of 50 mm were cored from the parent block at an identical orientation. Then, the cores were cut into a length of 50 mm (slender ratio = 1.0). To ensure efficient water injection and wave propagation, the cylinder ends were precision-ground to a flatness with a 0.02 mm tolerance and a perpendicularity within 0.001 rad relative to the axis. The processed specimen was also shown in Fig. 1. All specimens were saturated using the vacuum saturation method and immersed in distilled water prior to testing. This process consists of a 24-hour air extraction phase followed by a 48-hour water injection phase, which minimizes the influence of preferential flow paths and seepage time-dependency. In addition, the porosity of the specimens was further determined by nuclear magnetic resonance and some basic mechanical and physical parameters were pre-tested for reference, as listed in Table 1. It is worth pointing out that specimens with obvious defects or strange wave velocity values were excluded.

2.2 Experimental apparatus and principles

To conduct CHM loading, the modified triaxial SHPB system was employed (Chen et al., 2024; Wang et al., 2025c;

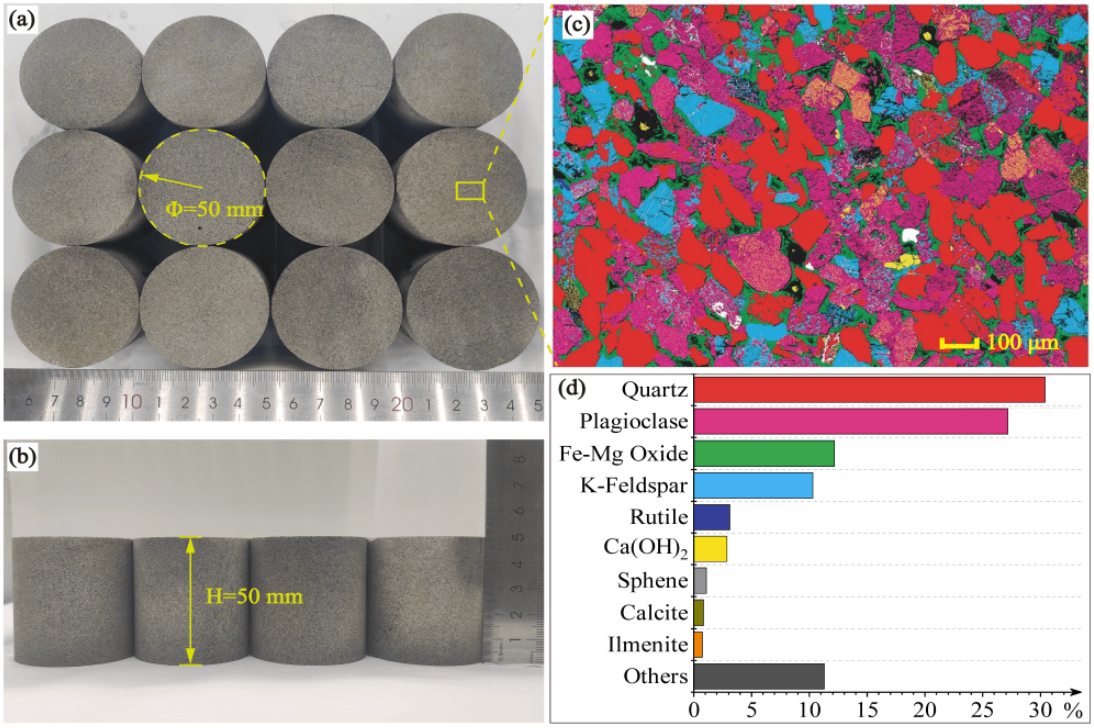

Fig. 1. (a)-(b) Prepared specimens, (c) resulting image of electron probe microscopic analysis, and (d) mineral component of the rock.

Table 1. Physical and mechanical parameters of the sandstone specimen.

Density (kg/m^3)	P-wave velocity (m/s)	Uniaxial compressive strength (MPa)	Brazilian tensile strength (MPa)	Young's modulus (GPa)	Poisson's ratio (-)	Porosity (%)
2,330	3,500	40.0	5.4	8.5	0.3	12

Wang et al., 2026). As illustrated in Fig. 2, the system primarily consists of a conventional SHPB configuration to realize stress wave loading, a confining loading unit to stimulate geostress, and a hydraulic loading unit to introduce a fluid field. Specifically, the basic SHPB includes a 50 mm diameter bar system comprising a striker, an incident bar, and a transmitted bar, all of which are constructed from high-strength maraging steel and feature a Young's modulus of 211 GPa and a P-wave velocity of 5,280 m/s. The launching device component, namely the air gun, can drive the striker to impact the incident bar to generate a stress wave by releasing the pressured air within 0.2 s. The stress wave is sensed by two pairs of strain gauges glued symmetrically on the incident and transmitted bars, respectively. These gauges form part of Wheatstone bridge circuits that convert the mechanical strain into electrical signals, which are subsequently amplified by a dynamic signal conditioner and recorded on a four-channel digital oscilloscope. To facilitate the stress equilibrium within the specimen, a C1100 copper disc is attached to the impact end as a pulse shaper (Wang et al., 2021b). The reflected compressive wave is converted into a tensile wave using a momentum trap technique to prevent multiple stress wave loading after each impact (Xia et al., 2008). The confining loading unit features a cylindrical vessel that surrounds the specimen to provide radial pressure, complemented by a piston-flange mechanism at the distal ends of the incident and transmitted bars for axial loading. Both pressure components are applied independently via a hydraulic system, with a maximum capacity of 100 MPa (Xu et al., 2024). The hydraulic loading unit comprises: (1) A dual-mode servo-controlled device capable of regulating both flow and pressure within 0.02 s, much longer than the duration of stress length to avoid overcompensation; (2) a connecting rod with a 1 mm diameter water channel and a circumferential groove at the specimen-contacting end to ensure uniform water distribution; and (3) an interconnected stainless-steel tube with the inner diameter of 1 mm. To establish a complete axial seepage channel, the incident bar was modified in a manner consistent with the connecting rod configuration at the specimen interface (cf. enlarged view of Fig. 2).

Prior to loading, two rubber rings were respectively equipped on the incident and transmitted bars, between which the saturated specimen is sandwiched coaxially. As shown in Fig. 3(a), a heat shrunk tube was wrapped on the rings and heat-contracted to completely isolate the specimen (Zhao, 2022; Wu et al., 2025). After that, the confining vessel was closed and filled with oil. The radial and axial pressures

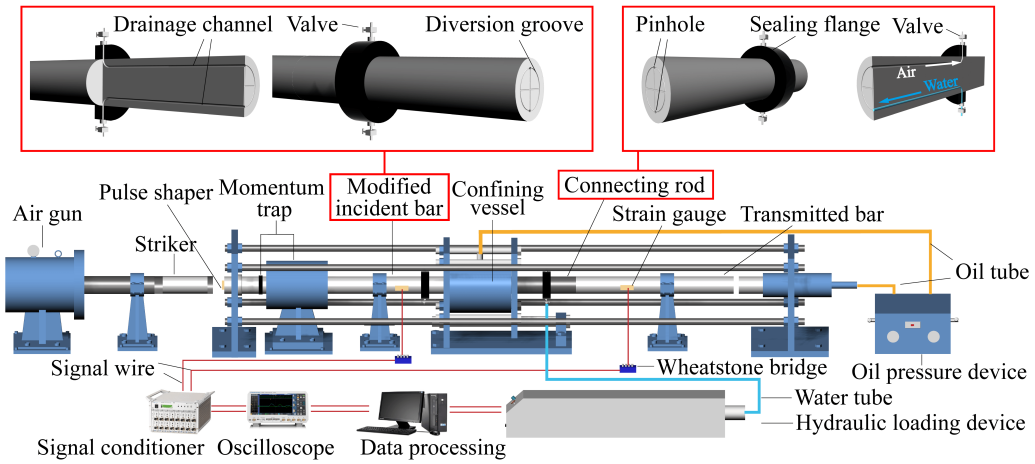

Fig. 2. Schematic of the CHM loading system.

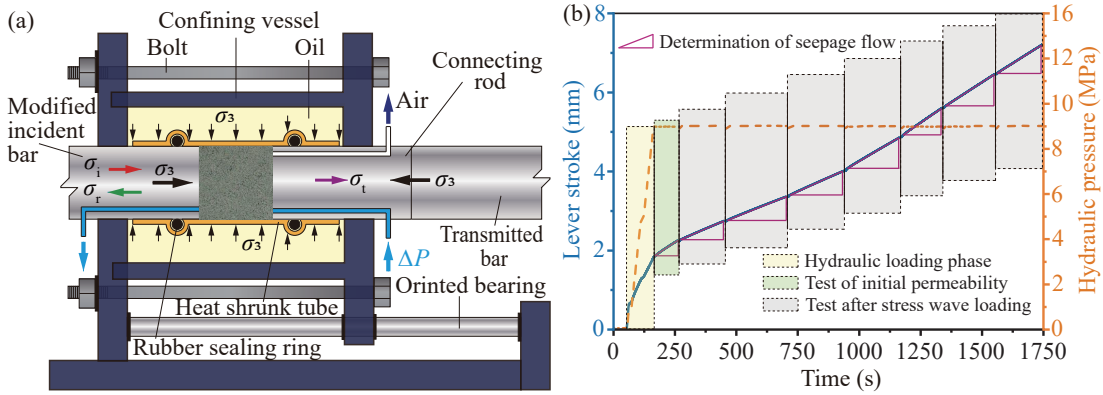

Fig. 3. (a) Rock specimen assembly and (b) determination of permeability from water injection information.

were then applied synchronously to the desired value, simulating a hydrostatic stress state (σ_3). Subsequently, the water was injected into the specimen from the transmitted end to reach a specific pressure, while the incident end remained exposed to the ambient atmosphere. A hydraulic pressure (ΔP) driving the axial water flow was thus established across the specimen under the differential water pressure between its two ends. It should be noted that, to prevent water leakage and maintain positive effective confining pressure, the hydraulic pressure was set below the confinement value ($\Delta P < \sigma_3$). After the water injection entered into a phase of stable seepage, i.e., stable water-injecting pressure and velocity, dynamic loading was performed with precise control. After each impact, the permeability of the specimen was measured under the consistent hydraulic and confining pressure following the re-stability of the water seepage. Assuming the water seepage within the specimen as a type of pipe seepage, the corresponding Reynolds number can be determined to fall within the laminar flow range, as reported in our previous work (Wang et al., 2025c). Then, the Darcy's law applies, and the *in-situ* permeability can be derived from the water-injecting information (Wang et al., 2025c):

$$k_N = \frac{V_N S \mu l_0}{\Delta P A_0} \tag{1}$$

where k_N represents the specimen permeability (md) after the N^{th} impact; S is the cross-sectional area (m^2) of the loading piston in the hydraulic loading device; V_N denotes the velocity (m/s) of the loading lever which can be determined from its displacement history, as shown in Fig. 3(b); A_0 and l_0 are the original cross-sectional area (m^2) and length of the specimen (m), respectively; μ refers to the viscosity coefficient (Pa·s) of water.

2.3 Stress wave loading of different energy input modes

In accordance with the principles of the one-dimensional wave theory, the amplitude of the stress wave is determined by the impact velocity and the pulse width is related to the length of the striker. The generation of stress waves with variable energies is enabled through the modulation of air pressure within the gas gun. In this study, the stress wave loading is characterized by the input energy, quantified as the integral of the incident bar's stress-strain curve (Wang et al., 2025c):

$$W_i = \int_0^t EAc_0\varepsilon_i^2 \mathrm{d}\tau \tag{2}$$

where W_i denotes the energy (J) carried by the incident stress wave; E and A are the Young's modulus (Pa) and cross-sectional area (m) of the bar, respectively; ε_i represents the incident strain history (-), c_0 denotes the wave velocity (m/s),

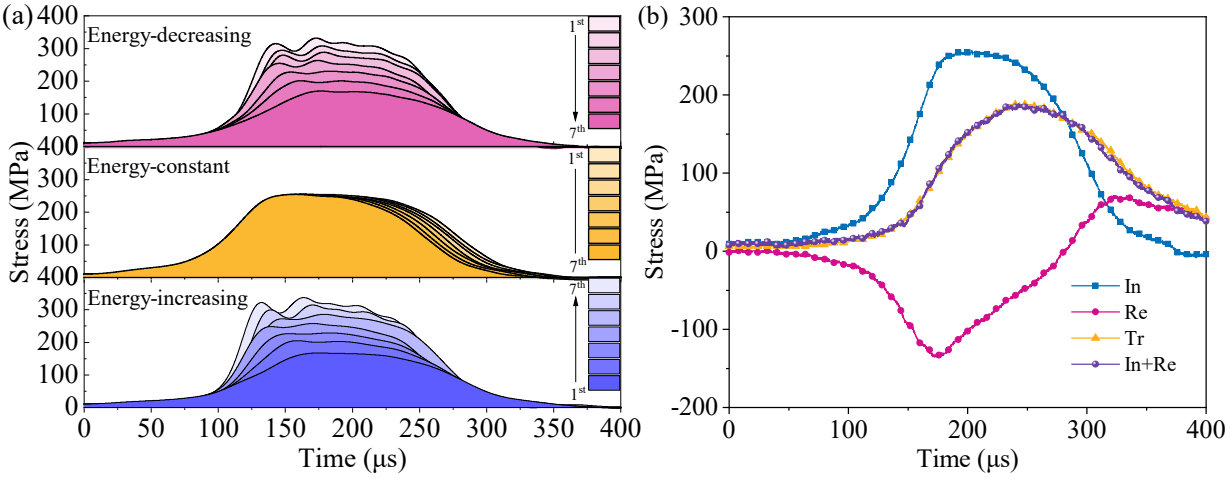

Fig. 4. (a) Impact design and (b) determination of stress equilibrium.

Table 2. Scheme of impact test.

Hydrostatic pressure (MPa)	Hydraulic pressure (MPa)	Launch air pressure (psi)	Total Energy input (J)	Test ID pattern
5	1, 2, 3, 4	6-18 (inc)	~1,800	5-inc-x
		12 (con)		5-con-x
		18-6 (dec)		5-dec-x
10	1, 3, 5, 7, 9	9-21 (inc)	~2,500	10-inc-x
		15 (con)		10-con-x
		21-9 (dec)		10-con-x
105	1, 3, 5, 7, 9, 11, 13	12-24 (inc)	~3,200	15-inc-x
		18 (con)		15-con-x
		24-12 (dec)		15-dec-x

Notes: 1 psi = 6.895 kPa; "inc", "con", and "dec" represent increasing, constant, and decreasing, respectively; the symbol "x" in Test ID denotes the hydraulic pressure value.

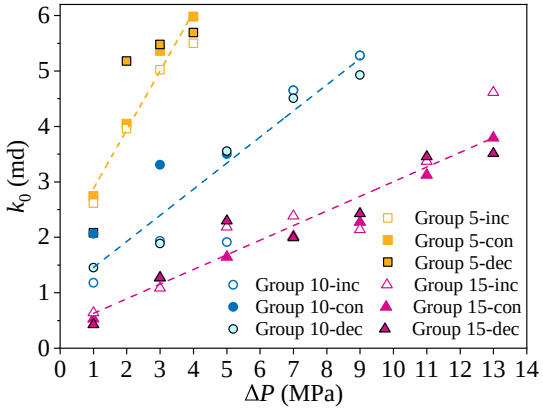

Fig. 5. Initial permeability under different coupled hydraulic-mechanical loading conditions.

t is the wave duration (s) and τ is the time interval (s). Preliminary experiments have determined that a copper disc measuring 9 mm in diameter and 1.5 mm in thickness is to be utilized for pulse shaping. Under each CHM loading condition, the specimen is subjected to seven instances of stress wave loading, with progressively increasing, constant, and decreasing energy, as illustrated in Fig. 4(a). Across the three energy input modes, the total input energy from the seven impacts remains constant under identical hydrostatic confining pressures. The experimental design is detailed in Table 2. Each test is numbered as a combination of the hydrostatic confinement, energy input mode, and hydraulic pressure. For example, 10-inc-5 indicates that the specimen is subjected to seven impact loads with progressively increasing energy at a confining pressure of 10 MPa and a hydraulic pressure of 5 MPa.

Furthermore, the stress equilibrium within the specimen was confirmed in every loading as required by the standard testing method to obtain the material dynamic response (Zhou et al., 2012). According to the one-dimensional stress wave theory, the forces subjected on the specimen ends can be calculated as (Wang et al., 2025b):

$$F_1 = EA(\varepsilon_i + \varepsilon_r) \tag{3}$$

$$F_2 = EA\varepsilon_t \tag{4}$$

where F_1 and F_2 are the force (N) applied on the incident and transmitted ends of the specimen; ε_i and ε_r represent the strain history (-) corresponding to the reflected and transmitted wave, respectively. A typical stress history is presented in Fig. 4(b), exhibiting a close alignment of the dynamic forces on both specimen ends (i.e., $F_1 \approx F_2$), indicating that the inertia effect can be neglected and the dynamic property determination is available.

3. Experimental results

3.1 Initial permeability

Prior to the stress wave loading, the initial permeability of the specimen was derived from water-injection measurements, as shown in Fig. 5. Owing to the inherent microcracks and pore connectivity within the rock matrix, the initial permeability

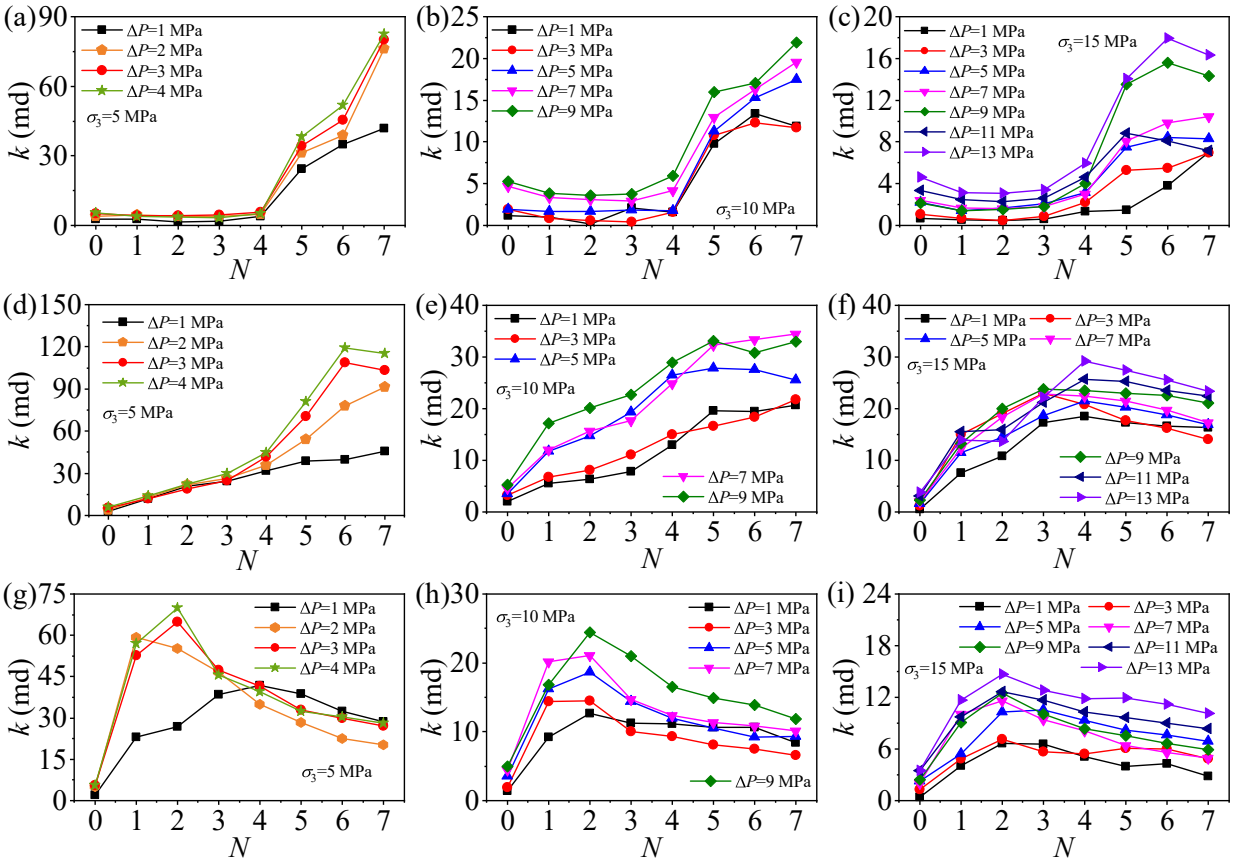

Fig. 6. Evolution of permeability after stress wave loading under (a)-(c) energy-increasing, (d)-(f) energy-constant, and (g)-(i) energy-decreasing mode.

remains finite rather than zero. Although the pore structures of natural rocks inevitably vary, the initial permeability values under identical CHM conditions exhibit minimal dispersion. This consistency verifies the homogeneity of the specimens and supports the reliability of the subsequent analysis of stress-wave effects. With increasing hydrostatic pressure, the initial permeability decreases proportionally because the seepage channels become compressed under confinement (Ning et al., 2022; Yu et al., 2022; Ghasemi et al., 2024). In contrast, an increasing hydraulic pressure produces an approximately linear increase in initial permeability. This behavior can be partly attributed to the elevated pore water pressure, which lowers the effective confining pressure on the rock skeleton and weakens the confinement-induced crack closure (Zhao, 2022). Additionally, the greater pressure difference across the specimen establishes a stronger pore-pressure gradient along the flow path, and the resulting water wedge force elevates the stress intensity factor at crack tips, promoting crack extension and widening the flow channels (Zhang et al., 2021b). As a result, permeability is enhanced. It is also notable that the initial permeability increases more markedly under lower confinement. Even when the effective confining pressure (i.e., the difference between hydrostatic and hydraulic pressures) is held constant, specimens subjected to higher absolute confinement exhibit lower initial permeability. This observation indicates that permeability is more sensitive to confining pressure than to hydraulic pressure alone, thereby demonstrating the coupled influence of hydraulic-mechanical loading.

3.2 Permeability evolution

The evolution of the specimen's inherent permeability under various CHM conditions and different stress wave loading modes is shown in Fig. 6. After seven impacts, the permeability shows a marked increase across all CHM conditions, which aligns with previous studies (Zhu et al., 2021; Chen et al., 2024; Wang et al., 2025c). However, under distinct CHM conditions and energy-input modes, the permeability evolution trends differ significantly.

Under the energy-increasing loading mode, as shown in Figs. 6(a), 6(b), and 6(c), the evolution of permeability can be divided into two stages. Taking Fig. 6(a) as an example, during the first four impacts, permeability remains nearly unchanged or slightly decreases, indicating that the specimen retains structural integrity. Low-amplitude loading compresses the porous structure, causing seepage channels to close and leading to reduced permeability. As the impact energy increases, permeability rises sharply after the 5th impact. This increase arises from the initiation and growth of cracks that connect previously isolated pores, which are accelerated by instantaneous loading (Yao et al., 2020; Zhao, 2022). However, this permeability enhancement is not strictly proportional to the energy input. Following the 6th and 7th impacts, permeabil-

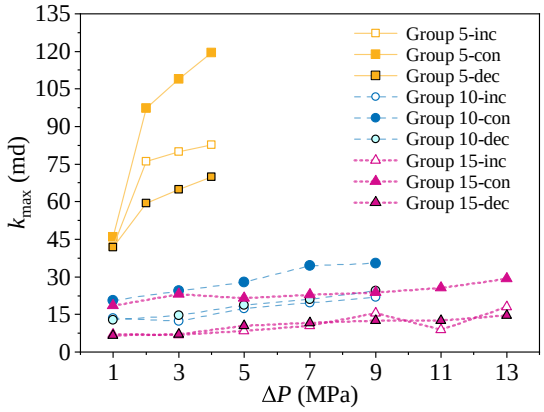

Fig. 7. Peak permeability during each loading series.

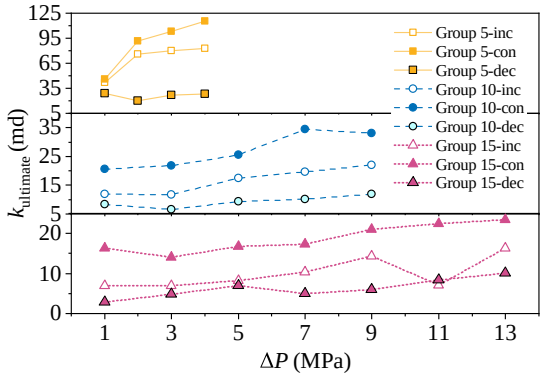

Fig. 8. Ultimate permeability after stress wave loadings.

ity exhibits only minor increases or even slight declines (Figs. 6(b) and 6(c)) under elevated hydraulic pressure. This behavior may result from the continuous sliding of rock fragments along existing macro-fracture surfaces, where uneven mineral grains undergo shear failure and form a fragmented shear zone (David et al., 2001; Heiland and Raab, 2001). Fragments and particles clog seepage channels, leading to a decrease in permeability. In contrast, under the energy-constant loading mode at lower confining pressures (Figs. 6(d) and 6(e)), permeability increases continuously but non-uniformly before reaching its peak. The first three impacts lead to gradual permeability enhancement at hydrostatic pressures of 5 MPa and 10 MPa, followed by more pronounced increases during the final four impacts. However, under 15 MPa confinement (Fig. 6(f)), permeability peaks after the fourth impact and subsequently declines. In the energy-decreasing loading mode (Figs. 6(g), 6(h), and 6(i)), this trend becomes more prominent across all CHM conditions. Permeability increases sharply during the first two impacts but gradually decreases thereafter.

In addition, the magnitude of permeability variation differs among loading modes and CHM conditions. For a given energy-input pattern, permeability enhancement is more pronounced under higher hydraulic pressures but remains minimal under high confining pressures. This trend is similar to that observed in initial permeability (k_0 in Fig. 5), indicating that CHM regulates permeability evolution throughout the stress wave loading process. Furthermore, despite the same total input energy at the same confinement level, the permeability evolution range varies markedly among loading modes. Overall, permeability exhibits the greatest enhancement under repeated stress wave loading with constant moderate energy, while the other two modes produce smaller but comparable ranges. For example, at a confining pressure of 10 MPa and a hydraulic pressure of 7 MPa (pink inverted triangles in Figs. 6(b), 6(e), and 6(h)), maximum permeability values of 19.55, 34.52, and 21.11 md are achieved under energy-increasing, energy-constant and energy-decreasing modes, respectively. Permeability reaches its peak after seven impacts in the energy-increasing mode (Fig. 6(b)), whereas it peaks in the energy-decreasing mode after only the first two impacts (Fig. 6(h)), suggesting that, for a comparable permeability enhancement effect, the energy-decreasing loadings achieves higher energy utilization efficiency than the energy-increasing loadings.

3.3 Peak and ultimate permeability

To further evaluate the permeability-enhancing effect of stress wave under different energy input paths, the peak permeability during each seven loadings was extracted and plotted in Fig. 7. The results indicate that, under all CHM conditions, the energy-constant loadings produce the most pronounced enhancement of rock permeability. Under a confining pressure of 5 MPa, the permeability-enhancing effects associated with the energy-increasing and energy-decreasing loading modes progressively weaken. As hydraulic pressure increases, peak permeability increases sharply with ΔP elevating to 2 MPa and then goes up slowly and linearly with hydraulic pressure. At higher confining pressures, however, the difference in permeability enhancement between the energy-increasing and energy-decreasing modes becomes minimal. Peak permeability for all loading modes exhibits nearly linear growth with increasing hydraulic pressure, and the nearly parallel trends suggest that the influence of hydraulic pressure on permeability enhancement is largely independent of the energy-input mode. Combined with earlier observations, this confirms that the permeability-enhancing effect of stress wave loading is jointly regulated by CHM conditions and energy-input patterns.

The ultimate permeability measured after each complete loading sequence was plotted in Fig. 8. Since permeability generally increases throughout the energy-increasing and energy-constant processes, in most cases, the ultimate permeability is identical to the peak value. However, under energy-decreasing impacts and under certain CHM conditions during energy-constant loading, permeability exhibits a declining trend in the later stage. Consequently, the final seepage characteristics vary markedly among different loading patterns. Under high confining pressure, the overlap in permeability among loading modes decreases. Within the tested CHM range, the energy-constant mode produces the highest ultimate permeability, while the energy-decreasing mode yields the lowest. Moreover, confining pressure and hydraulic pressure exert a weakening and strengthening effect on the final permeability, respectively. However, the strengthening effect of water pressure becomes less pronounced under high confining

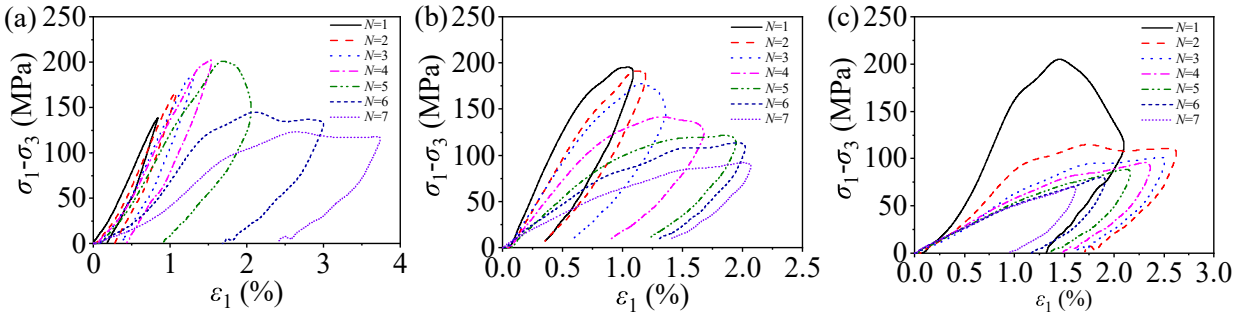

Fig. 9. Typical stress-strain relationships under specific CHM condition and (a) energy-increasing, (b) energy-constant, and (c) energy-decreasing loading modes.

pressure.

4. Analysis based on dynamic response

4.1 Dynamic stress-strain relationship and peak stress

To obtain an insight into the influence of different loading modes on permeability enhancement, crack development was analyzed in relation to the dynamic response of the specimens. With stress equilibrium achieved within the specimen, inertial effects become negligible, enabling reliable data reduction analysis. The application of the one-dimensional stress wave theory yields the dynamic stress-strain relationship (Wang et al., 2025b):

$$\sigma_1 - \sigma_3 = \frac{AE}{A_0}\varepsilon_t(t) - \sigma_3 \tag{5}$$

$$\varepsilon(t) = -\frac{2c_0}{l_0}\int_0^t \varepsilon_r(t)\,d\tau \tag{6}$$

where σ_1 denotes the total stress (Pa) experienced by the specimen; σ_3 is the stress (Pa) caused by the hydraulic confinement; $\sigma_1 - \sigma_3$ represents the stress (Pa) caused by stress wave loading.

To establish distinct dynamic responses for the three loading modes, the representative stress-strain curves for impacts conducted under 10 MPa confinement and 5 MPa hydraulic pressure were presented in Fig. 9, where the subgraphs correspond to the blue tringles in Figs. 6(b), 6(e), and 6(h), respectively. In the energy-increasing mode (Fig. 9(a)), the first four impacts produce gradually increasing peak stress and peak strain, with similar stress-strain shapes. A clear concave-up compaction stage appears at the onset of loading, and because the incident energy remains low, damage accumulation is minimal, resulting in strong overlap among successive loading paths. The elastic strain energy stored in the specimen is small and no evident plastic stage emerges. As this energy is rapidly released, the unloading modulus nearly equals the elastic modulus, indicating minimal structural degradation. From the 5th to 7th impacts, however, peak stress begins to decrease despite increasing input energy, reflecting intensified damage and progressive crack development. The elastic modulus reduces, plastic deformation becomes dominant, and a post-peak softening stage emerges, corresponding to a sharp rise in permeability (blue triangles in Fig. 6(b)). This is consistent with the fact that permeability is governed by fracture propagation. In contrast, under constant-energy loading, the peak stress decreases monotonically (Fig. 9(b)). Since the incident loads remain identical, the stress decline represents the weakening of load-bearing capacity. Continuous damage accumulation causes a gradual reduction in the elastic modulus and increasing plastic deformation. By the 4th impact, a pronounced post-peak softening stage forms, after which the stress-strain curves stabilize into nearly linear pr- and post-peak segments, indicating the presence of a dominant macro-crack. This stabilization coincides with a slight reduction in permeability (Fig. 6(e)), showing that after the major crack has formed, further loading contributes little to permeability enhancement. A similar trend appears in the energy-decreasing mode (Fig. 9(c)). In the first two higher-energy impacts, the stress-strain curves clearly exhibit compaction, elastic and plastic stages. As the impact energy diminishes, the peak stress continuously decreases. The second stress-strain curve resembles the 5th curve in the energy-increasing mode and the 4th curve in the constant-energy mode. During the following five lower-energy impacts, the curves behave similarly to the final three curves of the constant-energy mode. These correspond to the stage in which permeability declines (Fig. 6(h)), indicating that the specimen has already undergone substantial macro-crack formation. This parallel behavior across different loading modes further demonstrates the close correlation between permeability evolution and dynamic response: the development of macro-failure structures enhances seepage capacity, whereas fully formed fracture networks eventually stabilize under loading and even weaken the seepage property.

To further clarify the relationship between dynamic behavior and seepage properties, the peak stresses of specimens tested under a confinement of 10 MPa were extracted and are shown in Figs. 10(a), 10(b) and 10(c). In the energy-increasing impact series, the peak stress first rises and then declines, whereas it decreases consistently in the other two loading modes. The reduction in peak stress is relatively uniform in the energy-constant mode, while in the energy-decreasing mode, it exhibits a pronounced drop before transitioning to a gradual decline. Notably, the occurrence of maximum peak stress generally coincides with the onset of rapid permeability growth. For example, permeability remains low after the peak stress is reached in the energy-increasing impact series. However, the

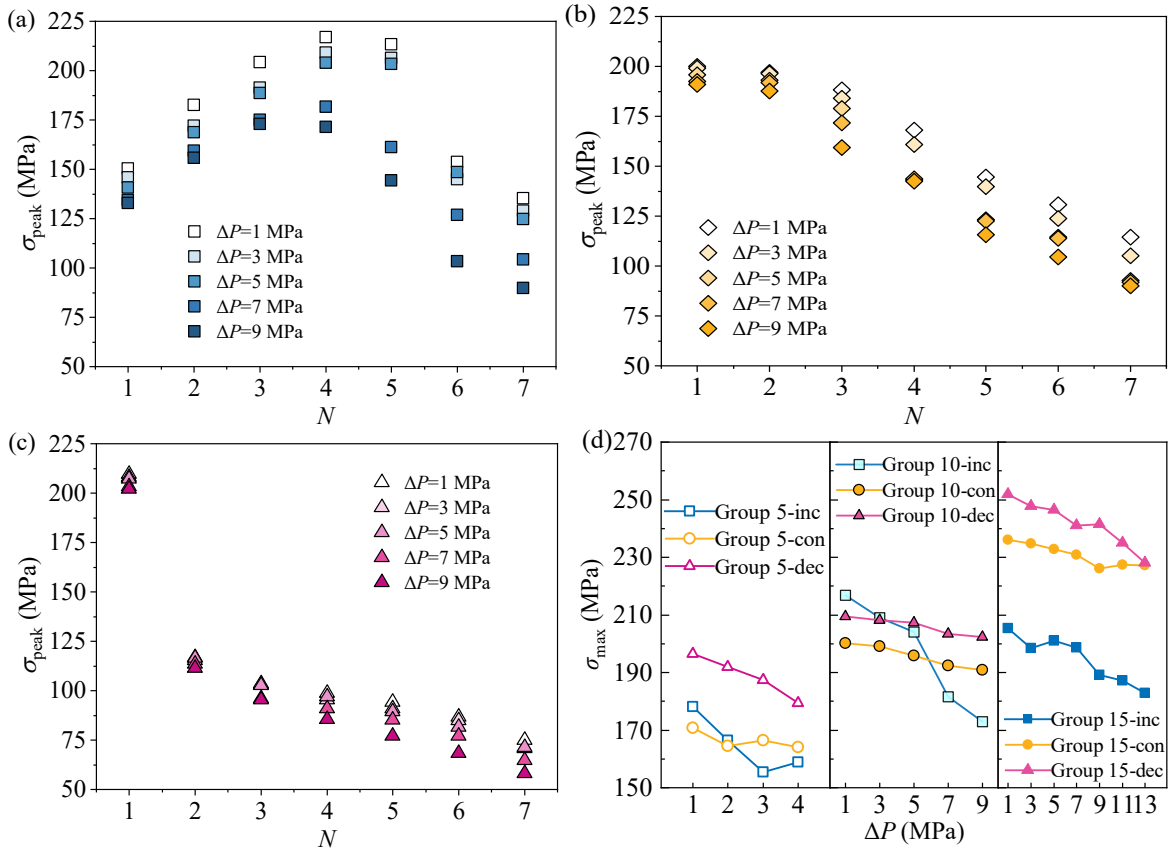

Fig. 10. Peak stresses of the specimen under (a) energy-increasing, (b) energy-constant, and (c) energy-decreasing modes of loadings at 10 MPa confinement, and (d) the maximum stress the specimen undergoes in the loading process.

subsequent stress reduction, together with the sharp increase in permeability, indicates that the specimen has entered a critical stage of damage accumulation. By contrast, in the other two loading modes, the maximum peak stress occurs during the first impact, accompanied by substantial plastic deformation and a marked post-loading increase in permeability. Similar trends have been reported in quasi-static triaxial compression tests, where seepage behavior correlated strongly with stress levels during cyclic loading and peak permeability appeared when primary cracks formed (Zhang et al., 2020; Bohnsack et al., 2021; Sheng et al., 2021; Zhang et al., 2021a). These observations suggest that regardless of the specific impact producing the peak stress, the simultaneous occurrence of maximum stress and permeability enhancement reflects the loss of load-bearing capacity preceding permeability growth.

Furthermore, increasing the hydraulic pressure has been widely shown to reduce peak stress during dynamic loading, as observed in SHPB tests on rocks with varying saturation levels (Kim and Changani, 2016), pore pressures (Zhao, 2022), and seepage gradients (Chen et al., 2024). Wang et al. (2025b) attributed this weakening to three reasons: reduced effective confinement, the water-induced degradation of particle cementation, and water-pressure-driven crack propagation. Importantly, the reduction in dynamic peak stress with increasing hydraulic pressure contrasts with the corresponding increase in permeability, further reinforcing their coupling through material damage. Fig. 10(d) summarizes the maximum stress sustained by each specimen within a loading series. It can be seen that higher confinement consistently yields greater maximum stresses. The specimen exhibits the strongest load-bearing capacity under the first impact in the energy-decreasing mode, which concentrates energy input early in loading. In contrast, the maximum stress in the energy-increasing mode is usually the lowest due to accumulated damage from preceding impacts. As a result, under identical CHM conditions, maximum stress does not scale proportionally with peak permeability.

4.2 Deformation characteristics

To explore the specimen damage, the deformation characteristics during stress wave loading were extracted. Fig. 11 presents the peak strains corresponding to the peak stresses presented in Fig. 10. In the energy-increasing mode (Fig. 11(a)), the peak strain associated with the maximum stress generally increases with impact number. Although peak stress decreases during the later impacts, the continuous growth in peak strain signifies the persistent development of cracks within the specimen. As porosity increases and more water enters the fracture network, the acoustic impedance decreases, reducing the peak stress that can be sustained (Zhang et al., 2025). A similar increasing trend in peak strain is observed in the energy-constant mode (Fig. 11(b)). However, in the energy-decreasing mode, the peak strain first rises and then declines with successive impacts. This trend reflects the

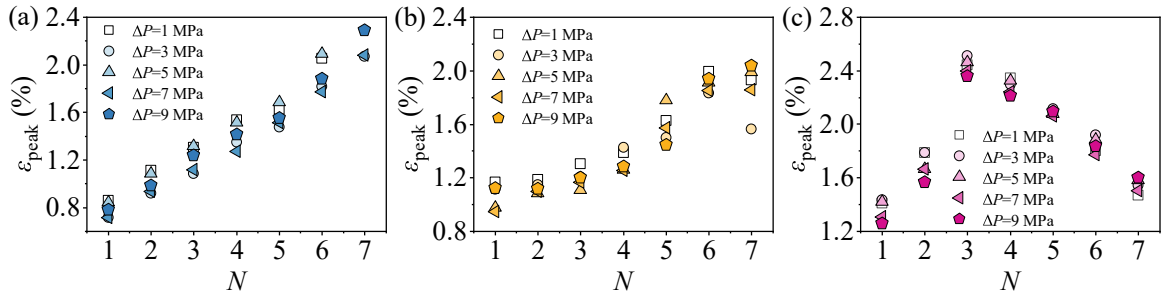

Fig. 11. Peak strain of the specimen during (a) energy-increasing, (b) energy-constant, and (c) energy-decreasing loading series.

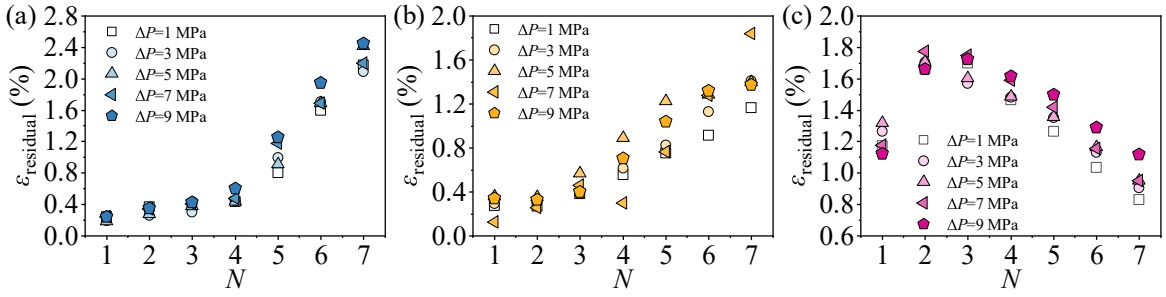

Fig. 12. Residual strain after each impact under various CHM conditions and (a) energy-increasing, (b) energy-constant, and (c) energy-decreasing loading modes.

combined effects of diminishing energy input and the evolving mechanical state of the specimen. As detailed in Section 4.1, the concentrated energy input during the initial impact induces macro-failure. In the post-failure loading stage, the progressive reduction in energy gradually diminishes the consolidation effect on the fractured specimen, leading to a continuous decrease in both specimen deformation and permeability. It is worth noting that the maximum peak strain occurs later than the maximum peak stress, i.e., the highest peak stress occurs in the first impact while the max strain is reached at the 3rd loading. This lag likely results from the concentrated energy input after the initial failure, which compacts the damaged specimen and produces a modest temporary increase in load-bearing capacity, a behavior also reflected in the residual strength (Fig. 9(c)) and the observed slight increment in permeability (Figs. 6(g), 6(h), and 6(i)). Besides, the effect of hydraulic pressure on the peak strain during specific loading periods fluctuates, consistent with triaxial SHPB experiments (Gong et al., 2019), and dynamic tests under variable water content (Zhou et al., 2016). Within a loading sequence, peak deformation is observed to be the greatest under energy-decreasing patterns and the smallest under energy-increasing patterns, a phenomenon that is analogous to that of peak stress. Consequently, peak strain has the potential to describe trends in permeability variation, while it cannot quantify the magnitude of permeability enhancement.

The residual strain after each impact under 10 MPa confinement is shown in Fig. 12. In both the energy-increasing and energy-constant loading series, the residual strain grows progressively with impact number. This behavior parallels the permeability evolution, indicating that the modest and gradually intensified loadings continually accumulate damage within the specimen. In contrast, residual strain in the energy-decreasing mode first increases and then decreases (Fig. 12(c)), which reflects the effect of decreasing incident energy. Specifically, the concentrated energy delivered during the first two impacts causes complete macro-failure and significantly reduces the elastic recovery of the specimen. Subsequent lower-energy impacts produce little additional damage and instead compact the fractured, porous medium, leading to a reduction in residual strain and permeability as the energy input declines. Notably, the peak residual strain generally coincides with the maximum permeability. This correspondence suggests a consistent evolution pattern between deformation and seepage properties, both governed by the development of macroscopic damage. However, residual deformation also fluctuates with increasing hydraulic pressure during certain loading periods, likely due to the non-uniform formation and interaction of crack networks.

To quantify the ultimate damage of the specimen, the accumulated residual strain for each loading sequence was calculated and shown in Fig. 13. The softening effect and crack-enhancing influence of pore water markedly increase overall deformation, with the accumulated strain rising in proportion to hydraulic pressure. Nevertheless, the accumulated deformation remains within a comparable range across different confining pressures, suggesting that confinement limits crack propagation caused by the higher energy input. Under specific CHM conditions, the specimen subjected to energy-decreasing impacts exhibits the largest total deformation, whereas the energy-constant mode retains the greatest proportion of the original specimen size. This trend contrasts with the variation in the ultimate permeability across loading modes (Fig. 8). Overall, the results reveal a negative correlation between de-

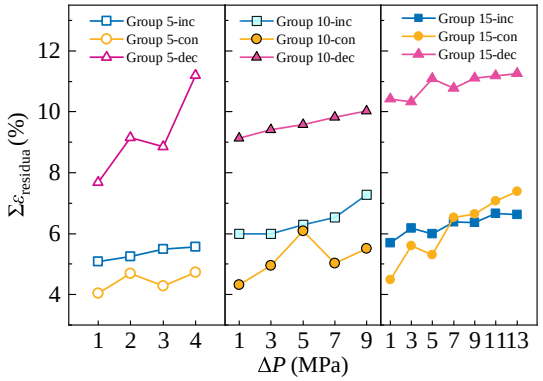

Fig. 13. Accumulated residual strain after each loading series.

formation and permeability enhancement within the examined energy range, highlighting the limited permeability growth achievable under continuous impact loading and offering a new insight into the coupled evolution of deformation, permeability and impact energy.

4.3 Energy dissipation

The dissipated energy, determined by the area enclosed within the stress-strain curve for a single loading cycle, was calculated and presented in Figs. 14(a), 14(b), and 14(c). It is evident that the dissipated energy shows an increasing trend comparable to that of permeability under both energy-increasing and energy-constant loading patterns. This consistency aligns with the test results from the energy-constant mode, where greater cumulative energy input and more loading cycles lead to sustained damage accumulation, supporting the use of dissipated energy as a damage indicator (Wang et al., 2025c). In the energy-increasing pattern, however, as energy becomes concentrated in the final few impacts, the still-intact specimen absorbs more energy, resulting in greater variability in energy dissipation. In contrast, under energy-decreasing loading, the dissipated energy exhibits a declining trend with increasing cycle number. According to energy conservation and the one-dimensional stress wave theory, this phenomenon can be attributed to the combined effect of reduced input energy and the decreased acoustic impedance of the specimen. The discrepancy between the trends in dissipated energy and permeability indicates that the former depends more strongly on the input energy level, and its utility as a damage descriptor is limited under non-constant energy loading conditions (Zhou et al., 2020). Fig. 14(d) further illustrates the total dissipated energy after each loading sequence. Overall, a higher hydraulic pressure correlates with a lower dissipated energy. Although increased permeability and deformation imply progressive cracking, the energy required for this process diminishes as water pressure differentials and seepage gradients actively promote cracking (Zhang et al., 2021b). Conversely, under elevated confining pressure, greater energy dissipation accompanies increased input energy, whereas permeability shows a decreasing trend. This inconsistency may be explained by the higher resistance of the constrained specimen to failure. Moreover, under low confining pressures, energy-constant loading resulted in the lowest energy dissipation, whereas under 15 MPa confining pressure, the smallest dissipation occurred during energy-increasing loading. This further underscores the limitation of using dissipated energy alone to characterize damage under variable energy loading paths.

5. Discussion

5.1 Mechanisms of permeability enhancement under different loading patterns

The experimental results demonstrate that the inherent permeability of rock is significantly enhanced by stress wave loading, and that this enhancement is strongly governed by the pattern of energy input rather than the total input energy alone. To elucidate the mechanisms underlying different permeability responses, the dynamic behavior of the specimen must be considered. It has been established that permeability does not increase continuously during repeated loadings or within a single complete loading cycle (Wang and Park, 2002; Zhang et al., 2007; Wang et al., 2025c). Once macro-failure forms and the permeability reaches its maximum, additional damage results in the re-compaction of the porous material, closure of flow pathways and thereby reduced permeability. Thus, differences in permeability evolution among loading modes arise from both the extent of crack development and the degree to which specimen integrity is preserved.

Under energy-constant loading, the incident stress, deformation and energy delivery are relatively moderate, and the specimen remains in the pre-failure stage throughout most of the loading sequence. As reflected by the gradual decrease in peak stress, together with the increase in peak strain, residual strain and dissipated energy, cumulative damage promotes crack development and leads to steady permeability enhancement. In contrast, the initial concentrated impact in the energy-decreasing mode causes rapid structural failure. Although permeability exhibits a slight increase due to the delayed hydraulic response relative to macro-crack formation, subsequent lower-energy loadings induce compaction rather than further cracking. The corresponding reductions in peak stress, residual strain and dissipated energy are accompanied by declining permeability. Thus, specimens experience both pre- and post-failure stages, whereas the peak permeability associated with dynamic strength is not captured because measurements were made after each loading. Ultimately, the permeability reaches the lowest value because compaction dominates the later stages. For energy-increasing loading, the largest energy is applied near the end of the sequence. The early low-amplitude impacts induce minimal structural damage. Although the peak stress rises due to increased incident energy, the residual strain remains small, reflecting crack closure rather than crack initiation. Consequently, permeability shows negligible change or even slight reduction. As energy inputs rise toward a certain threshold, accumulated damage becomes significant, residual deformation and energy dissipation increase, and the specimen approaches failure with a reduced energy requirement. The final one or two impacts typically destroy the specimen completely, although in some cases, the final impact partially compacts the already failed

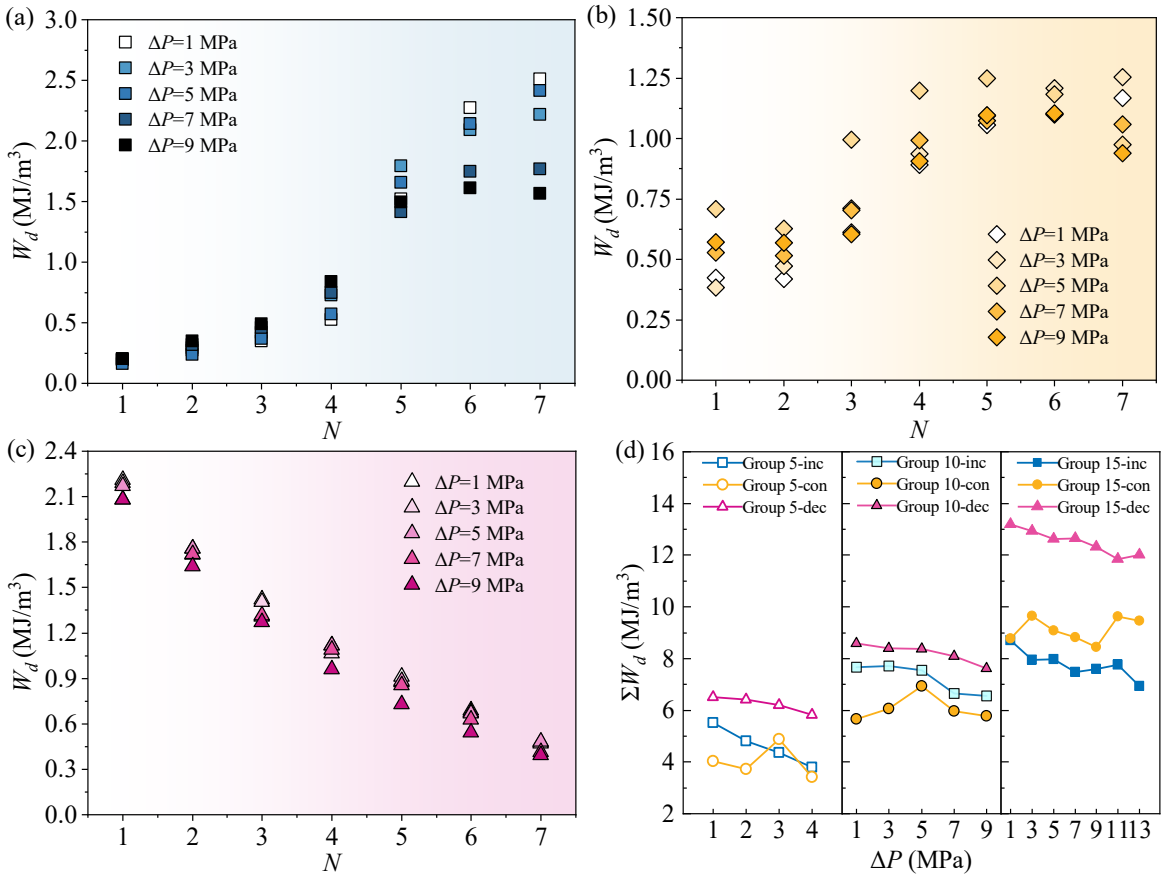

Fig. 14. Dissipated energy of the specimen under (a) energy-increasing, (b) energy-constant, (c) energy-decreasing loading modes at 10 MPa confinement, and (d) the corresponding accumulated dissipated energy in each loading series.

structure and induces a slight permeability decrease.

Overall, constant-energy loading achieves the greatest permeability enhancement because steady damage accumulation fosters crack interconnection prior to failure. In the other two modes, peak permeability generally follows the most energy-concentrated impact. However, the initial shocks in the energy-increasing mode have minimal effect and lead to energy wastage, whereas when both modes reach similar permeability levels, the energy-decreasing mode exhibits higher energy utilization efficiency.

5.2 Characterizing permeability and damage by a mechanical variable

Governed by the material damage properties, the evolutions of rock macroscopic mechanical response properties and the physical seepage properties are intrinsically correlated. Nevertheless, most dynamic variables derived from dynamic stress-strain analysis do not reflect permeability changes under all energy impact modes. This is primarily due to the fact that certain mechanical parameters are incapable of fully describing the entire loading-response process of the specimen. By contrast, permeability is a state variable that indicates the level of material damage after loading in this study, whereas peak stress and peak strain describe only the limit states reached during the process and therefore remain process variables (He et al., 2022). Moreover, the peak stress measured in experiments often does not represent the true load-bearing capacity (dynamic compressive strength). According to the stress wave propagation theory, the maximum stress achieved in the specimen depends jointly on its intrinsic damage characteristics, expressed through acoustic impedance, and on the amplitude of the incident stress. Hence, the evolutions of peak stress and dissipated energy are strongly affected by the energy input pattern (Zong et al., 2025). Nonetheless, it should be noted that this dependency does not weaken their relevance to permeability under energy-constant loading, where the influence is counteracted by the loading repetitiveness (Wang et al., 2025c). In this context, residual deformation serves both as a mechanical response parameter that describes the macroscopic behavior under loading and as an indicator of the internal damage state, exhibiting a trend consistent with permeability and therefore offering potential to characterize permeability changes.

5.3 Implications, limitations and prospects

The strong dependence of permeability evolution on loading mode suggests that optimal permeability stimulation can be achieved through controlled and moderate repeated impacts rather than extreme or irregular energy delivery. The findings offer a novel insight into the design of hydraulic stimulation,

dynamic permeability enhancement, and blast-induced seepage interventions in geotechnical and mining engineering. However, it should be noted that the dynamic tests were conducted on a homogenous specimen under conventional triaxial stress conditions. Therefore, the effects of complex geo-stress at depth and the joint nature of the engineering rock warrant further investigation. Future work should also focus on quantifying damage evolution through acoustic emission or micro-CT imaging to validate the relationships among deformation, crack and permeability established herein. Moreover, dynamic numerical simulations that incorporate nonlinear CHM coupling will facilitate an enhanced comprehension of fracture connectivity and allow the optimization of dynamic loading strategies.

6. Conclusions

This study employed a modified SHPB system to apply controllable stress-wave loading to green sandstone specimens under various CHM conditions. Each specimen was subjected to seven impacts with identical total input energy but while following increasing decreasing, or constant energy-input patterns. *In-situ* permeability was measured after each impact, and dynamic responses were analyzed to correlate permeability evolution with damage characteristics. The main conclusions are summarized as follows:

1) Permeability is significantly enhanced by stress-wave loading, with distinct evolution patterns observed under different energy-input modes. Under increasing-energy and constant-energy loading at low confinement, permeability exhibits progressive growth throughout the loading sequence. Under decreasing-energy loading and under repeated loading at higher confinements, permeability generally increases first and then undergoes a slight reduction.
2) Permeability enhancement is jointly regulated by pre-applied CHM conditions and dynamic loading. Hydraulic pressure promotes permeability via facilitating crack propagation, and increasing seepage gradients reduce load-bearing capacity while amplifying ultimate deformation. In contrast, hydrostatic confinement closes cracks and inhibits their development, leading to diminished permeability.
3) Stress wave loading with modest, constant input energy produces the strongest permeability enhancement, followed by energy-increasing loading, whereas energy-decreasing loading yields the weakest enhancement. These differences arise from the timing of specimen integrity loss, after which subsequent impacts may primarily induce compaction rather than further fracture development.
4) Permeability evolution cannot be reliably characterized using peak stress, peak strain or dissipated energy, because these parameters either fail to represent the full loading-response history or depend strongly on the energy-input sequence. In contrast, residual deformation reflects cumulative material damage and exhibits a strong positive correlation with permeability, demonstrating its potential as a mechanical indicator for permeability characterization.

Acknowledgements

This work was supported by the National Natural Science Foundation of China (Nos. 42377147 and 42141010).

Conflicts of interest

The authors declare no competing interest.

References

Bohnsack, D., Potten, M., Freitag, S., et al. Stress sensitivity of porosity and permeability under varying hydrostatic stress conditions for different carbonate rock types of the geothermal Malm reservoir in Southern Germany. Geothermal Energy, 2021, 9(1): 15.

Chen, R., Zhao, G., Xu, Y., et al. Coupled hydraulic-mechanical experimental system for evaluating dynamic mechanical and transport behaviors of deep rocks. Experimental Mechanics, 2024, 64(6): 895-911.

Chen, W., Maurel, O., Reess, T., et al. Experimental study on an alternative oil stimulation technique for tight gas reservoirs based on dynamic shock waves generated by Pulsed Arc Electrohydraulic Discharges. Journal of Petroleum Science and Engineering, 2012, 88-89: 67-74.

David, C., Menendez, B., Zhu, W., et al. Mechanical compaction, microstructures and permeability evolution in sandstones. Physics and Chemistry of the Earth, Part A: Solid Earth and Geodesy, 2001, 26(1): 45-51.

Duan, Z., Zhang, Y., Yang, F., et al. Research on controllable shock wave technology for *in-situ* development of tar-rich coal. Energy, 2024, 288: 129706.

Fan, C., Sun, H., Li, S., et al. Research advances in enhanced coal seam gas extraction by controllable shock wave fracturing. International Journal of Coal Science & Technology, 2024, 11: 39.

Ghasemi, S., Khamehchiyan, M., Taheri, A., et al. The effect of cyclic loading parameters on the physical, mechanical, and microcracking behavior of granite. Engineering Geology, 2024, 332: 107475.

Gong, F., Si, X., Li, X., et al. Dynamic triaxial compression tests on sandstone at high strain rates and low confining pressures with split Hopkinson pressure bar. International Journal of Rock Mechanics and Mining Sciences, 2019, 113: 211-219.

He, J., Tang, M., Gao, R., et al. Damage-permeability analysis of pretensioned spun high strength concrete pipe piles based on stochastic damage model. Engineering Failure Analysis, 2022, 140: 106578.

Heiland, J., Raab, S. Experimental investigation of the influence of differential stress on permeability of a lower permian (rotliegend) sandstone deformed in the brittle deformation field. Physics and Chemistry of the Earth,

Part A: Solid Earth and Geodesy, 2001, 26(1): 33-38.

Jiang, H., Yang, H., Pan, R., et al. Performance and enhanced oil recovery efficiency of an acid-resistant polymer microspheres of anti-CO_2 channeling in low-permeability reservoirs. Petroleum Science, 2024, 21(4): 2420-2432.

Jiang, Z., Yu, S., Deng, H., et al. Investigation on microstructure and damage of sandstone under cyclic dynamic impact. IEEE Access, 2019, 7: 133145-133158.

Kim, E., Changani, H. Effect of water saturation and loading rate on the mechanical properties of Red and Buff Sandstones. International Journal of Rock Mechanics and Mining Sciences, 2016, 88: 23-28.

Kluge, C., Blöcher, G., Hofmann, H., et al. The stress-memory effect of fracture stiffness during cyclic loading in low-permeability sandstone. Journal of Geophysical Research: Solid Earth, 2021, 126(10): e2020JB021469.

Kozhevnikov, E., Turbakov, M., Riabokon, E., et al. Rock permeability evolution during cyclic loading and colloid migration after saturation and drying. Advances in Geo-Energy Research, 2024a, 11(3): 208-219.

Kozhevnikov, E. V., Turbakov, M. S., Riabokon, E. P., et al. Apparent permeability evolution due to colloid migration under cyclic confining pressure: On the example of porous limestone. Transport in Porous Media, 2024b, 151(2): 263-286.

Lei, Y., Liu, J., Zhang, S., et al. Contrast test of different permeability improvement technologies for gas-rich low-permeability coal seams. Journal of Natural Gas Science and Engineering, 2016, 33: 1282-1290.

Liu, Y., Dai, F. A review of experimental and theoretical research on the deformation and failure behavior of rocks subjected to cyclic loading. Journal of Rock Mechanics and Geotechnical Engineering, 2021, 13(5): 1203-1230.

Maurel, O., Reess, T., Matallah, M., et al. Electrohydraulic shock wave generation as a means to increase intrinsic permeability of mortar. Cement and Concrete Research, 2010, 40(12): 1631-1638.

Mullakaev, M. S., Abramov, V. O., Abramova, A. V. Development of ultrasonic equipment and technology for well stimulation and enhanced oil recovery. Journal of Petroleum Science and Engineering, 2015, 125: 201-208.

Ning, Z., Xue, Y., Li, Z., et al. Damage characteristics of granite under hydraulic and cyclic loading–unloading coupling condition. Rock Mechanics and Rock Engineering, 2022, 55(3): 1393-1410.

Ranjith, P. G., Zhao, J., Ju, M., et al. Opportunities and challenges in deep mining: A brief review. Engineering, 2017, 3(4): 546-551.

Sheng, M., Mabi, A., Lu, X. Study on permeability of deep-buried sandstone under triaxial cyclic loads. Advances in Civil Engineering, 2021, 2021: 6635245.

Wang, C., Shen, H. R., Sun, L. H. Evolution law of fractured rock permeability under cyclic loading and unloading. International Journal of Geomechanics, 2025a, 25(7): 04025124.

Wang, J., Dai, F., Yan, Z., et al. Dynamic response of sandstone under hydro-mechanical coupling: macroscopic behavior and microscopic mechanism. International Journal of Rock Mechanics and Mining Sciences, 2026, 197: 106342.

Wang, J., Xue, Q., Du, X., et al. Study on the unplugging technology through electric explosion controllable shock wave. Journal of Energy Resources Technology, 2021a, 143(5): 053005.

Wang, J., Park, H. D. Fluid permeability of sedimentary rocks in a complete stress–strain process. Engineering Geology, 2002, 63(3): 291-300.

Wang, S., Xu, Y., Xia, K., et al. Dynamic fragmentation of microwave irradiated rock. Journal of Rock Mechanics and Geotechnical Engineering, 2021b, 13(2): 300-310.

Wang, Z., Yue, T., Zhao, G., et al. Dynamic properties of deep rocks under different seepage gradients: Experimental investigation and theoretical modeling. Journal of Rock Mechanics and Geotechnical Engineering, 2025b, https://doi.org/10.1016/j.jrmge.2025.08.035. (in Press)

Wang, Z., Zhao, G., Xie, Y., et al. Permeability enhancement of reservoir rocks loaded by repeated low-amplitude stress waves. International Journal of Rock Mechanics and Mining Sciences, 2025c, 194: 106243.

Wen, M., Harpers, N., Inskip, N. F., et al. Mechanical responses and permeability evolution in porous sandstones under cyclic loading conditions: Implications for subsurface hydrogen storage. Rock Mechanics and Rock Engineering, 2025, 58(9): 10643-10673.

Wu, B., Zhao, G., Xu, Y., et al. Dynamic compressive characteristics of a green sandstone under coupled hydraulic-mechanical loading: Experiments and theoretical modeling. Journal of Rock Mechanics and Geotechnical Engineering, 2025, 17(1): 126-138.

Xia, K., Nasseri, M. H. B., Mohanty, B., et al. Effects of microstructures on dynamic compression of Barre granite. International Journal of Rock Mechanics and Mining Sciences, 2008, 45(6): 879-887.

Xu, W., Qu, X., Zeng, T., et al. Mechanical and permeability properties of granite under hydro-mechanical coupled triaxial cyclic loading. Physics of Fluids, 2025, 37(5): 056604.

Xu, Y., Fu, Y., Wang, C., et al. Dynamic rock tensile failure under hydrostatic pressure analyzed with wavelet transform of acoustic emission signals. Engineering Fracture Mechanics, 2024, 306: 110206.

Yan, L., Yi, W., Liu, L., et al. Blasting-induced permeability enhancement of ore deposits associated with low-permeability weakly weathered granites based on the split Hopkinson pressure bar. Geofluids, 2018, 2018: 4267878.

Yao, W., Xu, Y., Xia, K. Damage evolution during rock pulverization induced by dynamic compressive loading. Journal of Geophysical Research: Solid Earth, 2020, 125(5): e2020JB019388.

Yu, M., Liu, B., Chu, Z., et al. Permeability, deformation characteristics, and damage constitutive model of shale under triaxial hydromechanical coupling. Bulletin of Engineering Geology and the Environment, 2022, 81(3): 85.

Zhang, J., Standifird, W. B., Roegiers, J. C., et al. Stress-dependent fluid flow and permeability in fractured media: From lab experiments to engineering applications. Rock

Mechanics and Rock Engineering, 2007, 40(1): 3-21.

Zhang, L., Tan, T., Wang, E., et al. Evolutionary characteristics and correlations between deformation energy and strain in anthracite coal during stress wave-induced catastrophes. Engineering Geology, 2025, 347: 107931.

Zhang, T., Liu, Y., Yang, K., et al. Hydromechanical coupling characteristics of the fractured sandstone under cyclic loading-unloading. Geofluids, 2020, 2020: 8811003.

Zhang, Y., Yu, T., Zhang, T., et al. Experimental investigation on permeability in fractured rock under different pressure conditions. Acta Geodynamica et Geomaterialia, 2021a, 18(4): 415-428.

Zhang, Z., Zhang, Q., Duan, K., et al. Experimental study on the mechanical and permeability behaviors of limestone under hydro-mechanical-coupled conditions. Bulletin of Engineering Geology and the Environment, 2021b, 80(4): 2859-2873.

Zhao, G. L., Li, X., Xu, Y., et al. A modified triaxial split Hopkinson pressure bar (SHPB) system for quantifying the dynamic compressive response of porous rocks subjected to coupled hydraulic-mechanical loading. Geomechanics and Geophysics for Geo-Energy and Geo-Resources, 2022, 8(1): 29.

Zhao, L. Mechanism of permeability enhancement in coal under repetitive strong shock waves. Arabian Journal of Geosciences, 2022, 15(3): 222.

Zhou, H., Wang, X., Zhang, L., et al. Permeability evolution of deep coal samples subjected to energy-based damage variable. Journal of Natural Gas Science and Engineering, 2020, 73: 103070.

Zhou, Y., Xia, K., Li, X., et al. Suggested methods for determining the dynamic strength parameters and mode-I fracture toughness of rock materials. International Journal of Rock Mechanics and Mining Sciences, 2012, 49: 105-112.

Zhou, Z., Cai, X., Cao, W., et al. Influence of water content on mechanical properties of rock in both saturation and drying processes. Rock Mechanics and Rock Engineering, 2016, 49(8): 3009-3025.

Zhu, Q., Li, D., Wang, W. Mechanical behavior and permeability evolution of sandstone with confining pressure after dynamic loading. Geomechanics and Geophysics for Geo-Energy and Geo-Resources, 2021, 7(3): 81.

Zong, Z., Feng, Y., Chen, F., et al. Effects of multi-scale wave-induced fluid flow on seismic dispersion, attenuation and frequency-dependent anisotropy in periodic-layered porous-cracked media. Petroleum Science, 2025, 22(2): 684-696.